Supporting Information

Tailored design, synthesis, and catalytic aspects of mononuclear *cis*- dichloro copper(II) complexes with simple DPA derived tridentate ligands and their biomimicking activities

Arabinda Muley,† Kalai Selvan Karumban,† Sadananda Kumbhakar, Shobhit Mathur, Indrajit Roy, Anushka Verma, Manoj Kumar Kumawat and Somnath Maji*

Department of Chemistry, Indian Institute of Technology Hyderabad, Kandi, Sangareddy 502284, Telangana, India

†These authors contributed equally to this work.

Email address: smaji@chy.iith.ac.in (Somnath Maji)

*Corresponding author

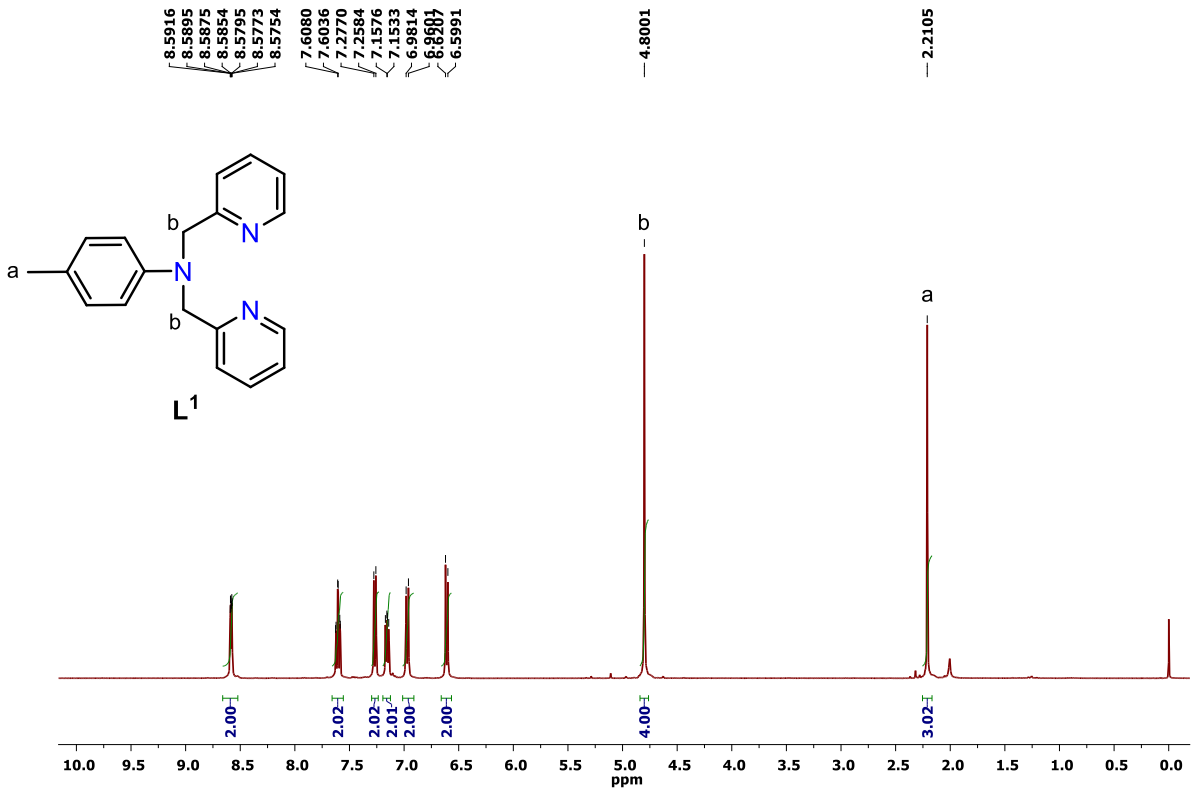

Fig. S1. ^{1}H NMR of **L^{1}** in $CDCl_3$ at room temperature.

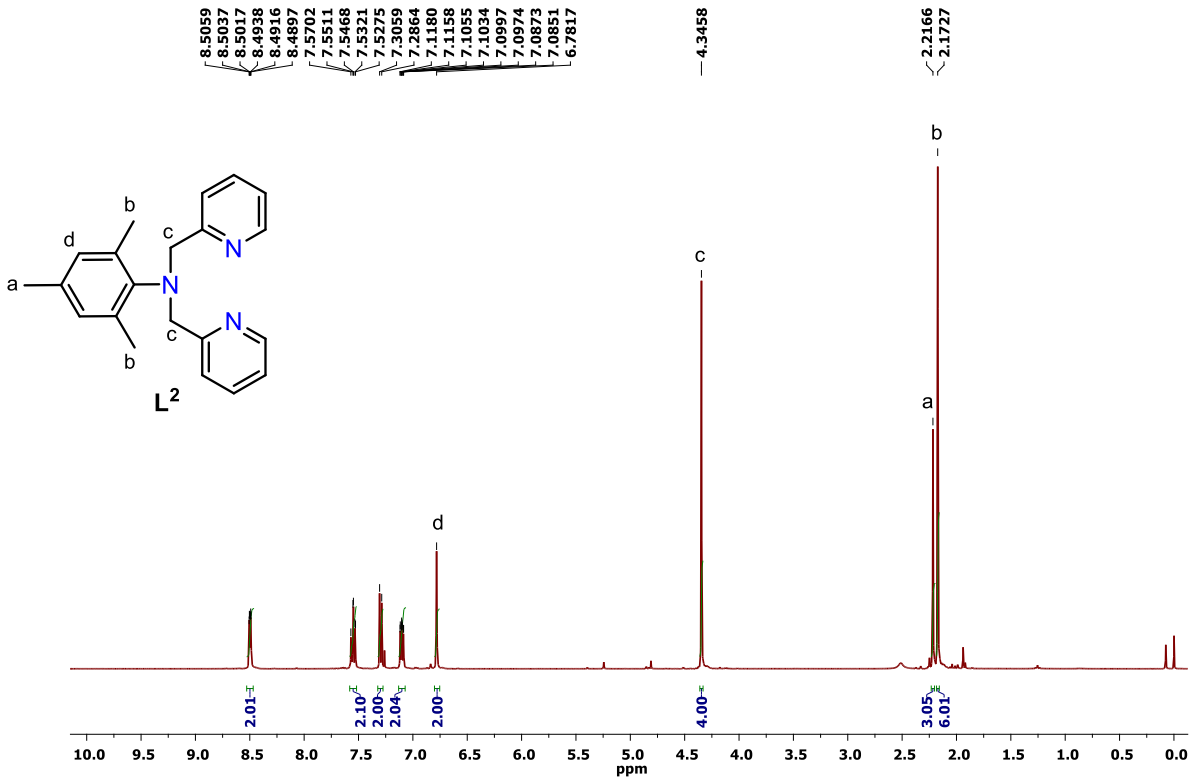

Fig. S2. ^{1}H NMR of **L^{2}** in $CDCl_3$ at room temperature.

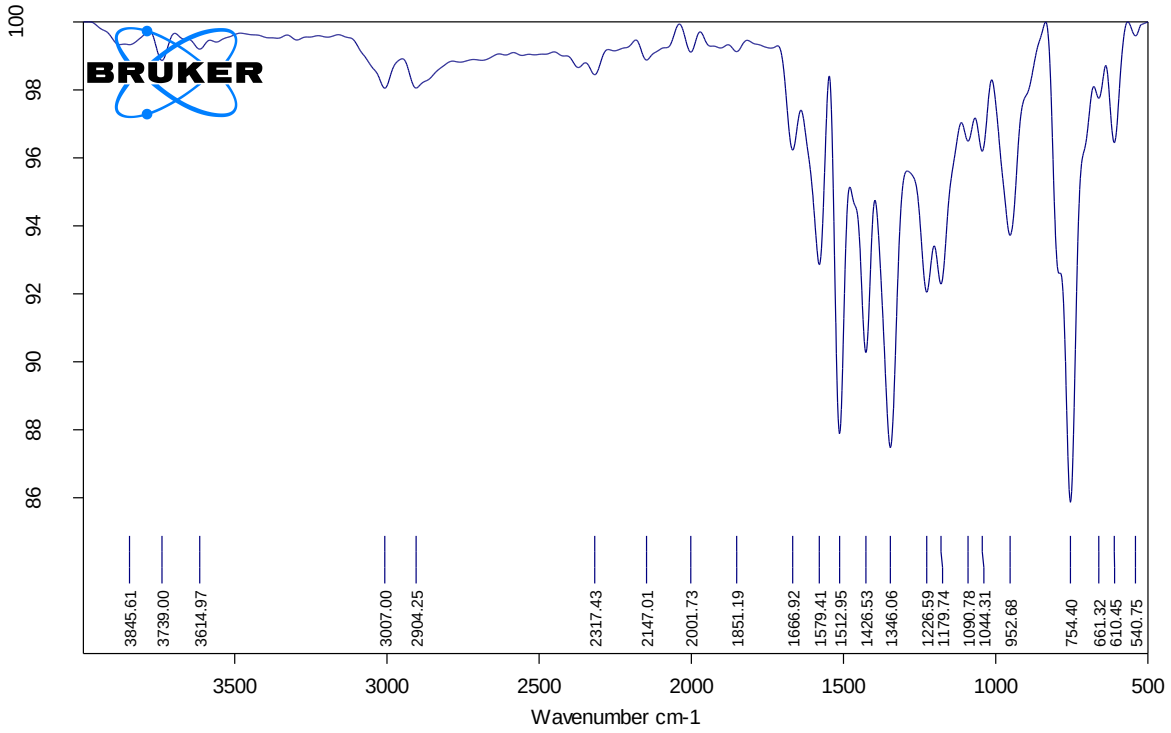

Fig. S3. FT–IR (Solid) spectrum of **L**[1].

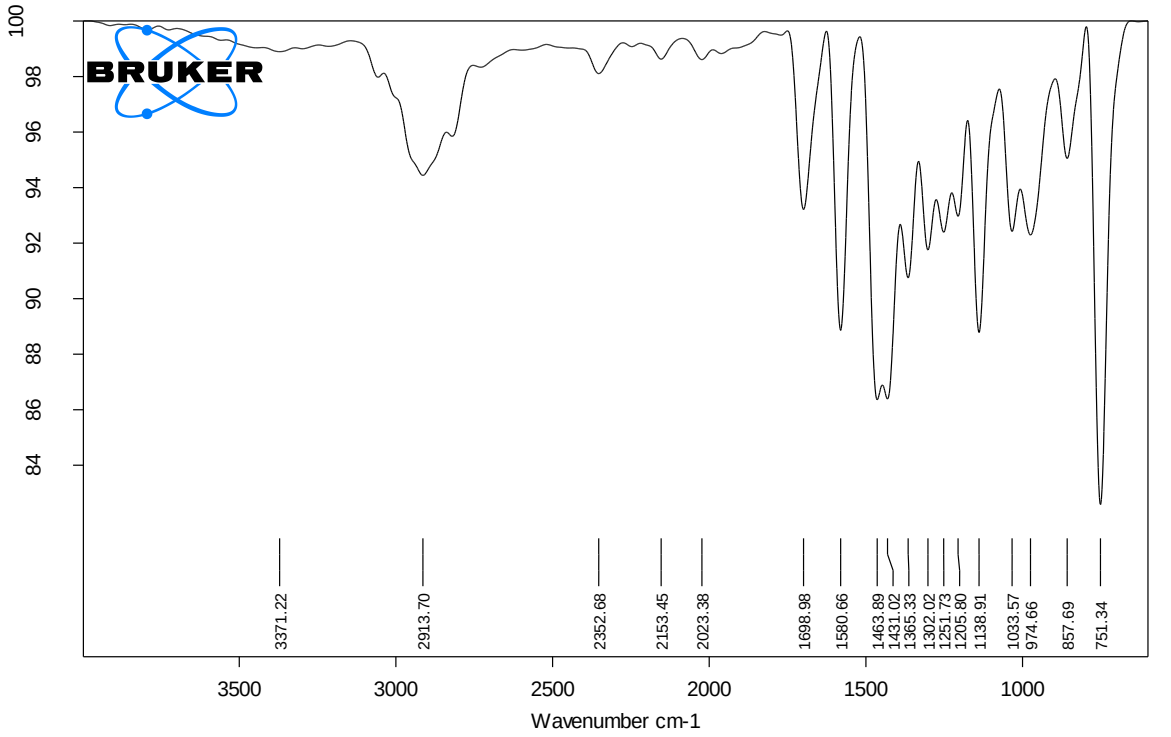

Fig. S4. FT–IR (Solid) spectrum of **L**[2].

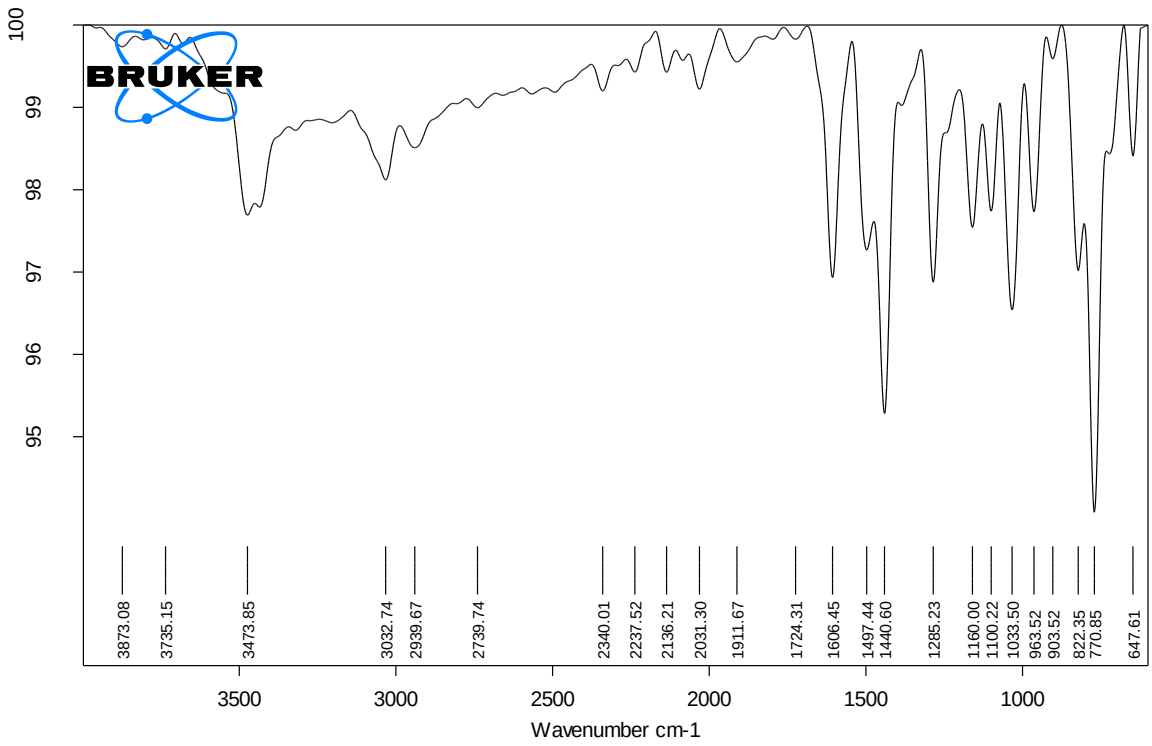

Fig. S5. FT–IR (Solid) spectrum of **1**.

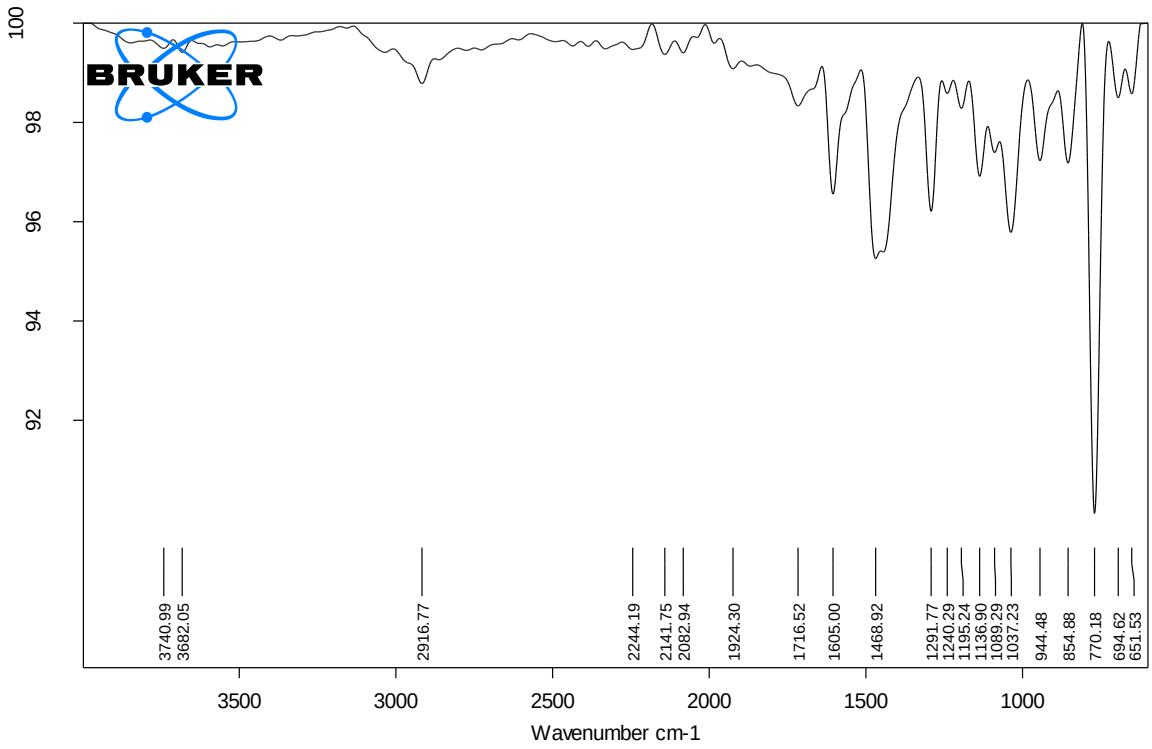

Fig. S6. FT–IR (Solid) spectrum of **2**.

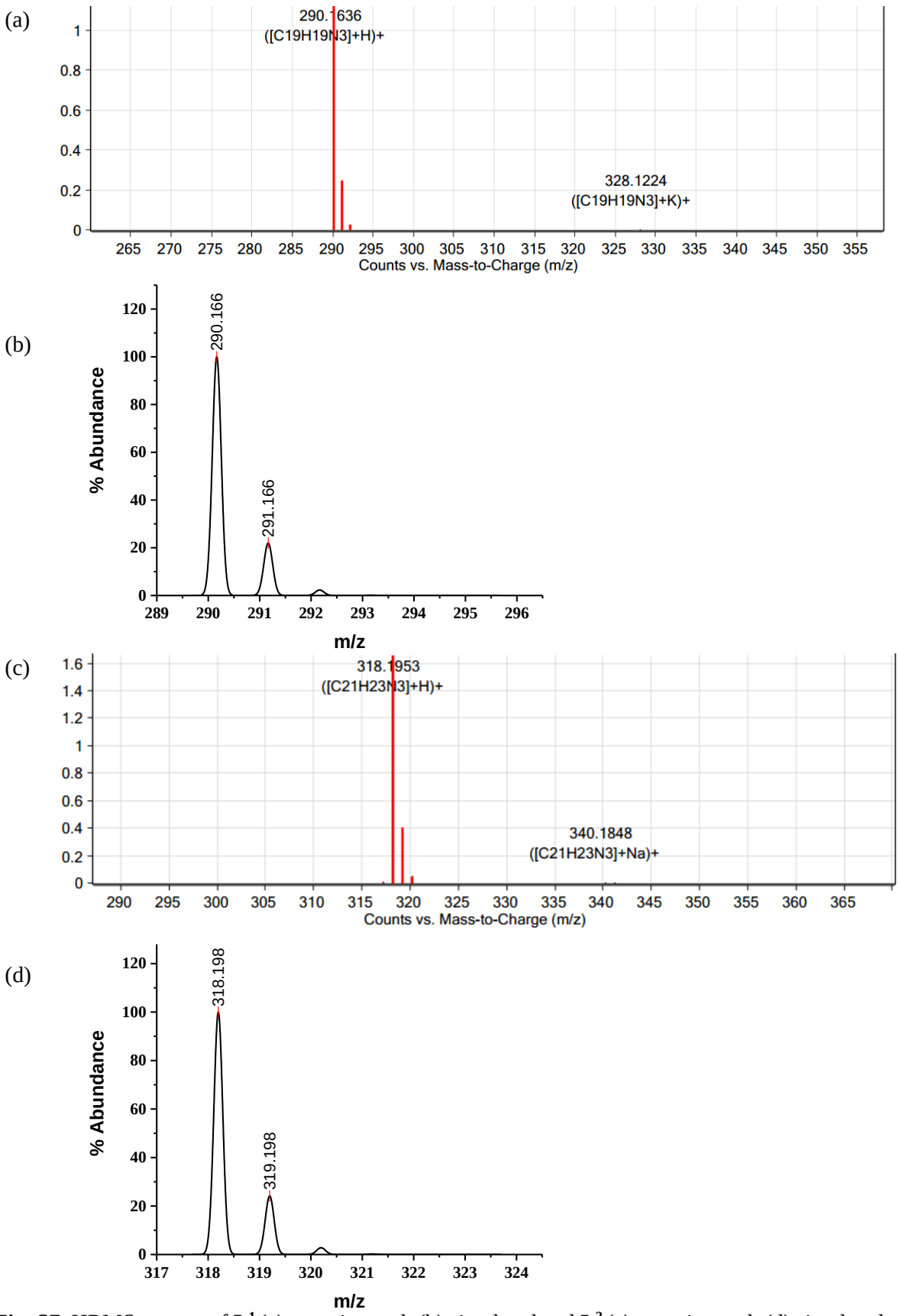

Fig. S7. HRMS spectra of $\mathbf{L^1}$ (a) experimental, (b) simulated and $\mathbf{L^2}$ (c) experimental, (d) simulated.

(a)

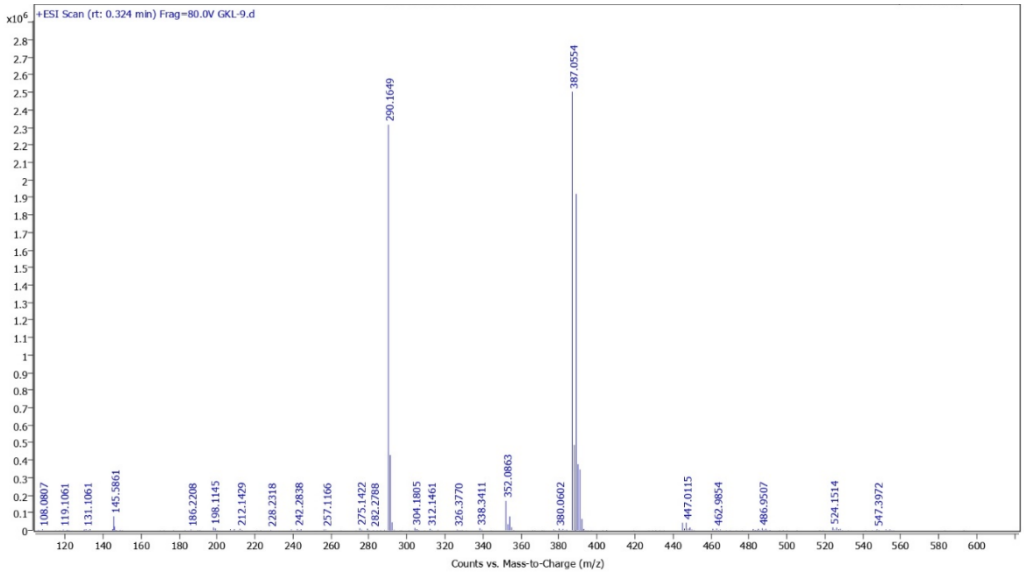
+ESI Scan (rt: 0.324 min) Frag=80.0V GKL-9.d
x10^6
387.0554
290.1649
108.0807
119.1061
131.1061
145.5861
186.2208
198.1145
212.1429
228.2318
242.2838
257.1166
275.1422
282.2788
304.1805
312.1461
326.3770
338.3411
352.0863
380.0602
447.0115
462.9854
486.9507
524.1514
547.3972
Counts vs. Mass-to-Charge (m/z)

(b)

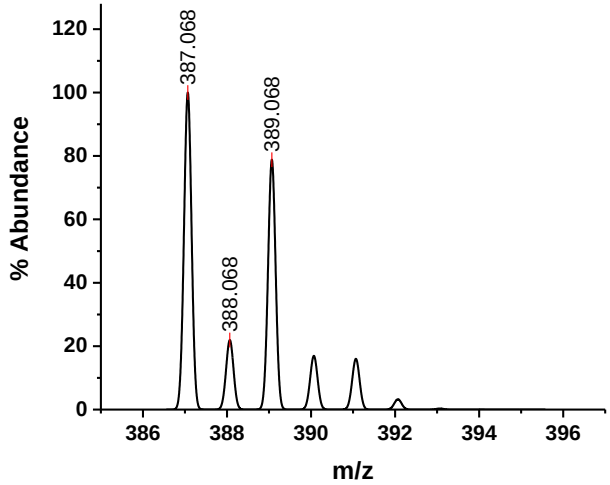
% Abundance
387.068
388.068
389.068
m/z

(c)

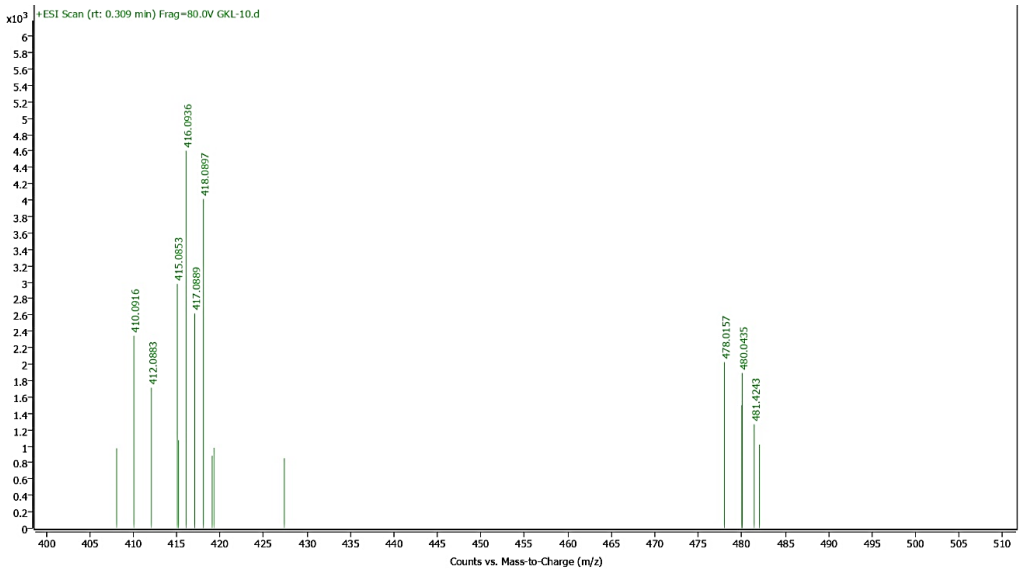
+ESI Scan (rt: 0.309 min) Frag=80.0V GKL-10.d
x10^3
410.0916
412.0883
415.0853
416.0936
417.0869
418.0897
478.0157
480.0435
481.4243
Counts vs. Mass-to-Charge (m/z)

(d)

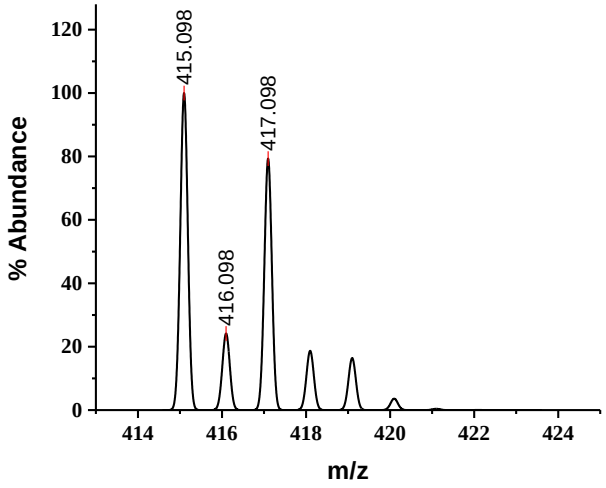

Fig. S8. HRMS spectra of **1** (a) experimental, (b) simulated and **2** (c) experimental, (d) simulated.

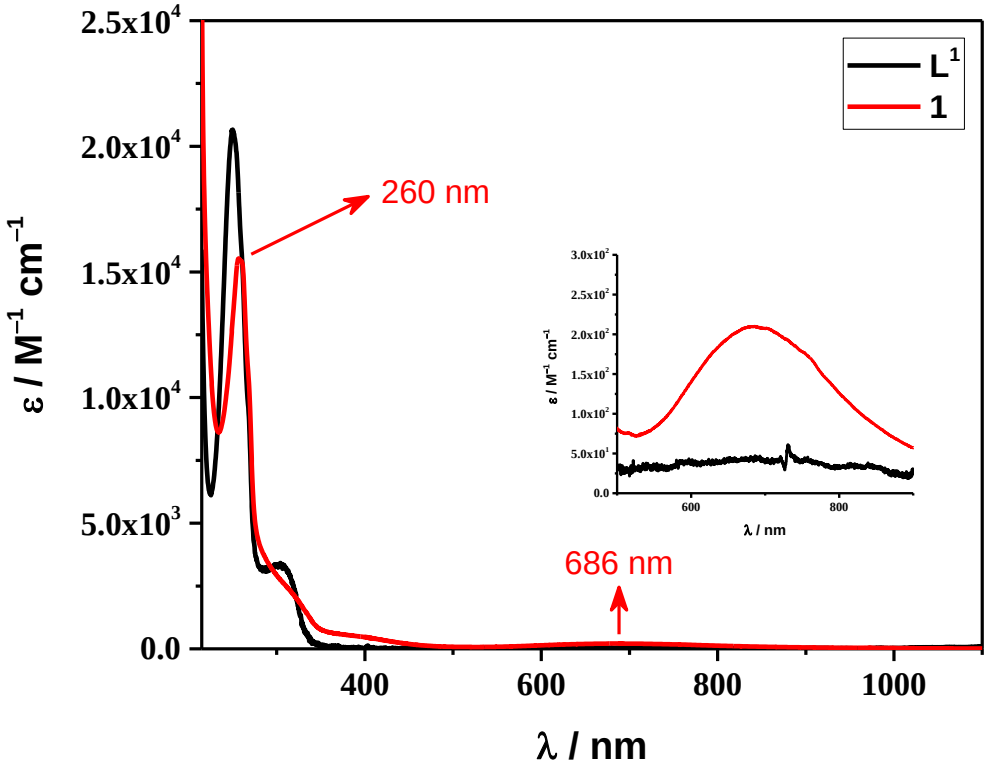

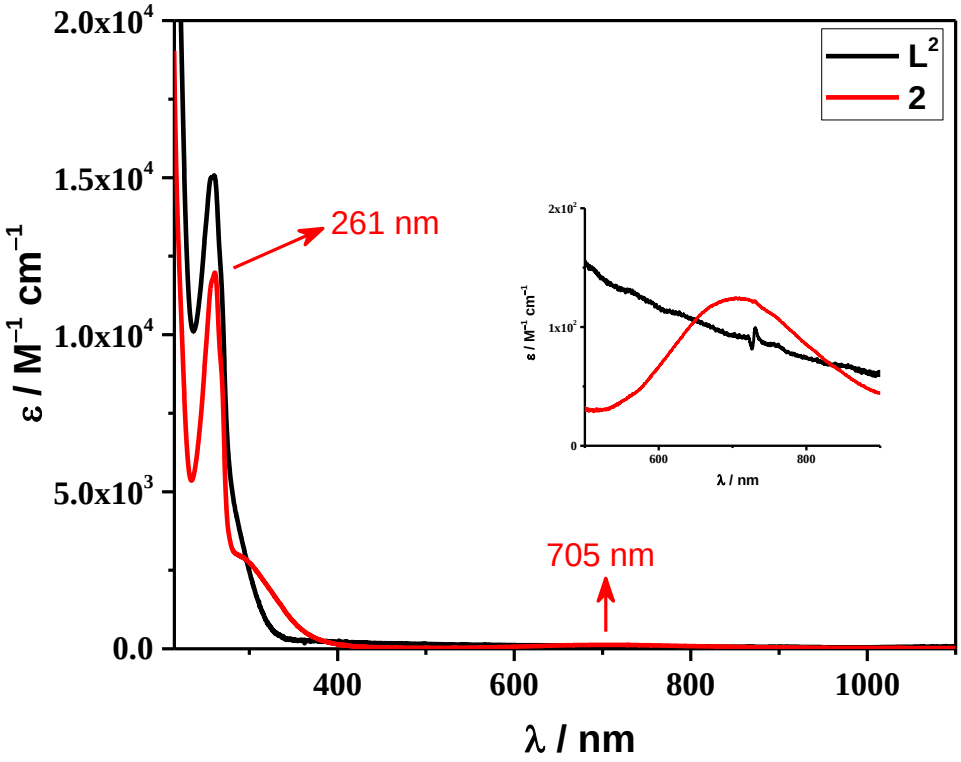

Fig. S9. Electronic spectra of **L**[1], **1** (top) and **L**[2], **2** (bottom) in methanol at room temperature.

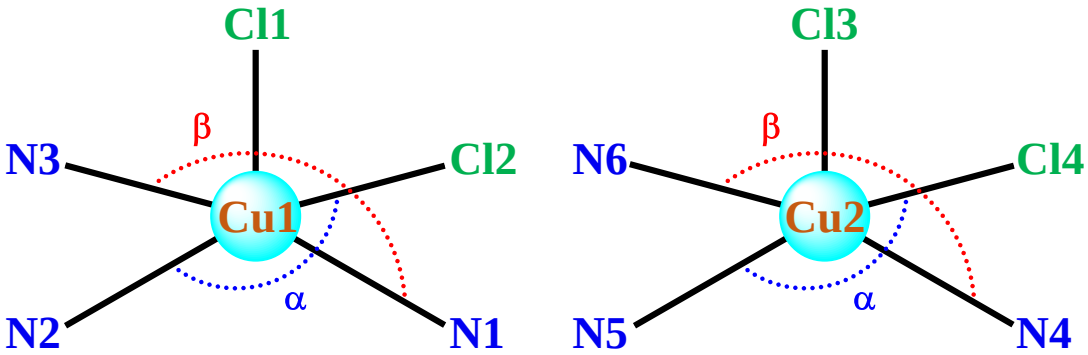

β = 162.9, α = 146.0 **1**

β = 158.39, α = 149.64 **2** (Cu1) β = 158.26, α = 130.64 **2** (Cu2)

Fig. S10. Schematic representation of **1** and **2**

(a)

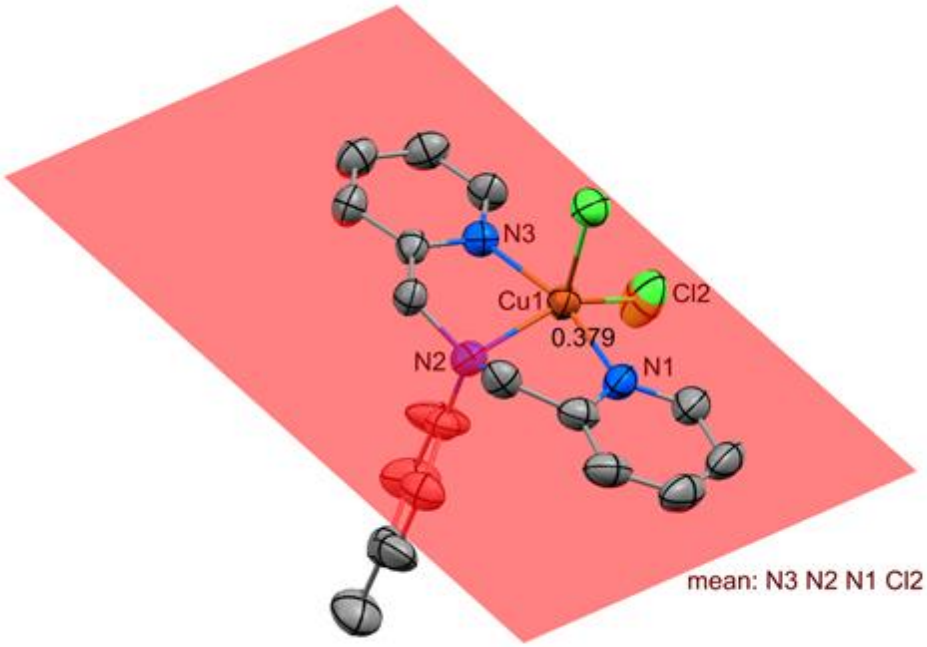
N3
Cu1
Cl2
0.379
N2
N1
mean: N3 N2 N1 Cl2

(b)

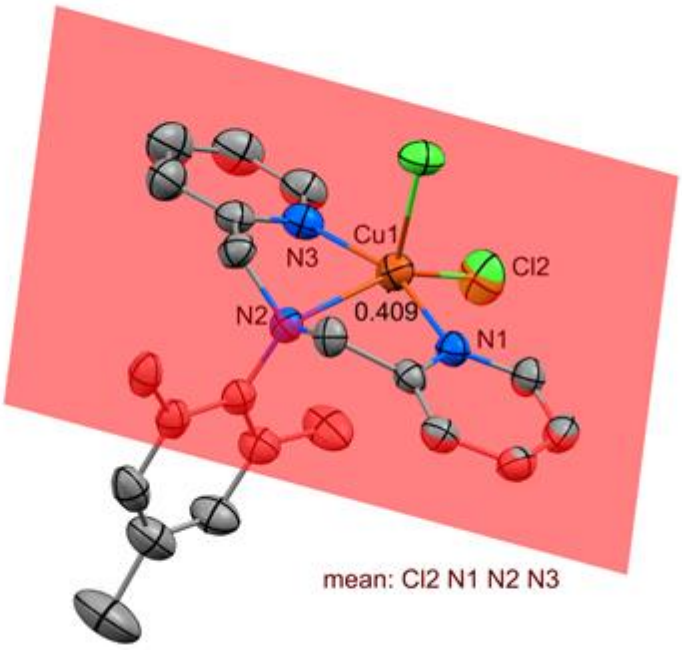
Cu1
N3
Cl2
N2
0.409
N1
mean: Cl2 N1 N2 N3

(c)

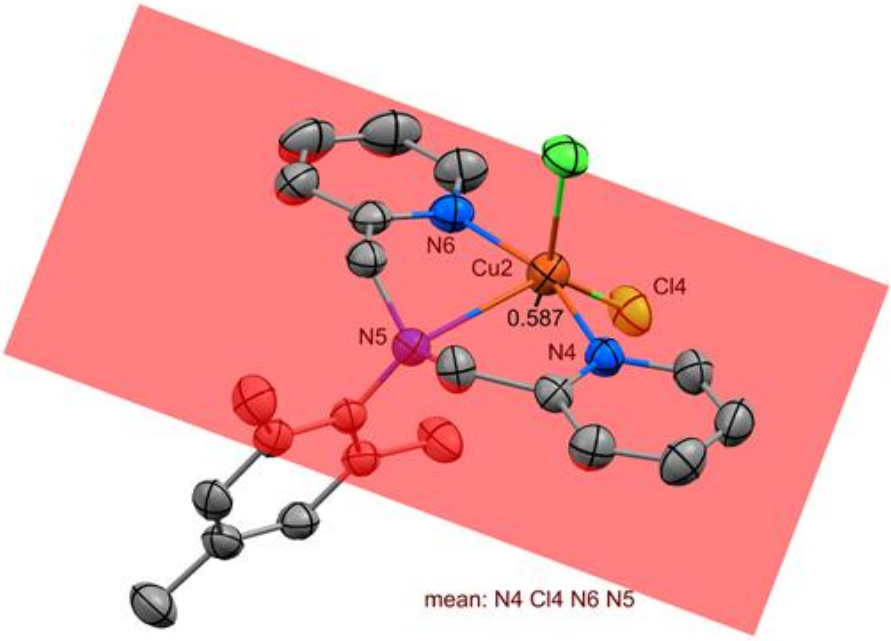

Fig. S11. The mean plane of copper ion sitting position in (a) **1** and (b) Cu1 center of **2** and (c) Cu2 center of **2.**

(a)

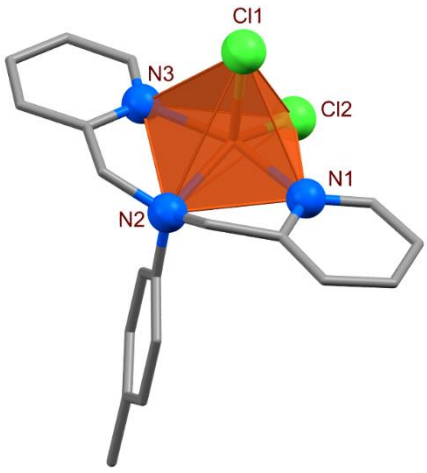

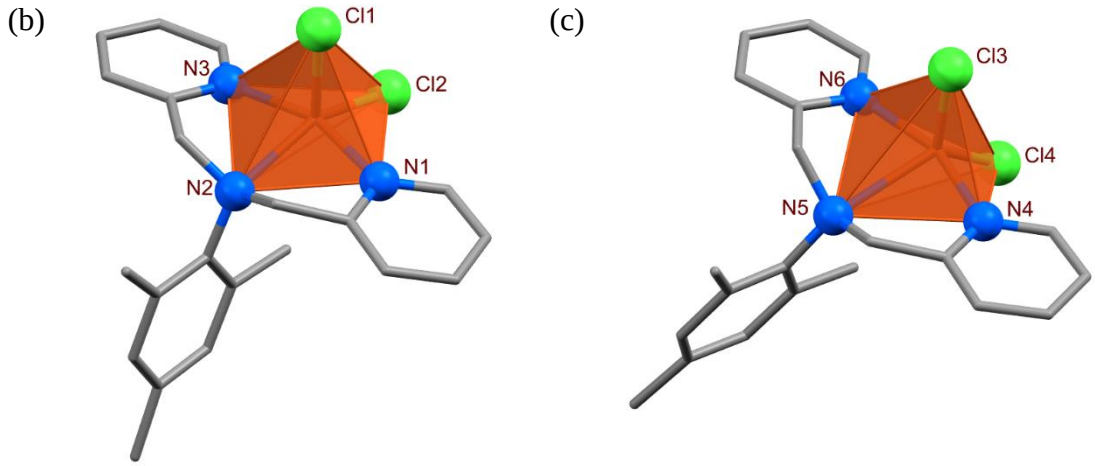

Fig. S12. The polyhedron view of (a) **1** and (b) Cu1 center and (c) Cu2 center of **2**.

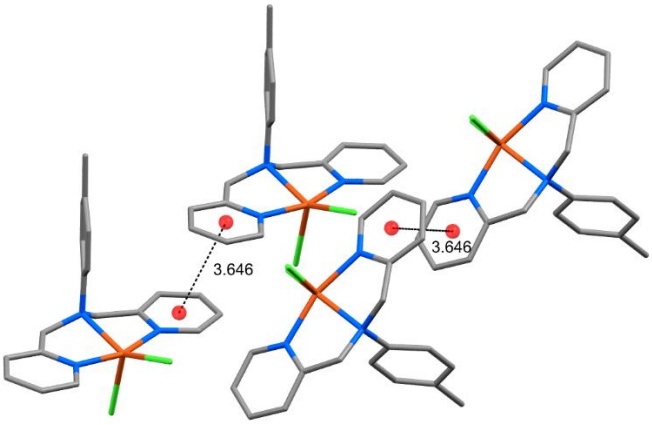

Fig. S13. π–π stacking present in the crystal structures of **1**.

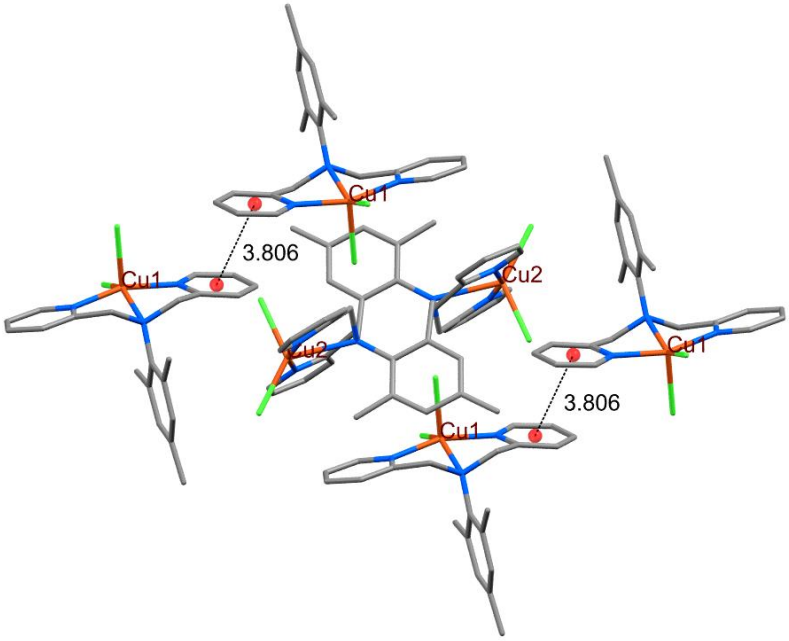

Fig. S14. π–π stacking present in the crystal structures of **2** between Cu1 centers.

(a) (b)

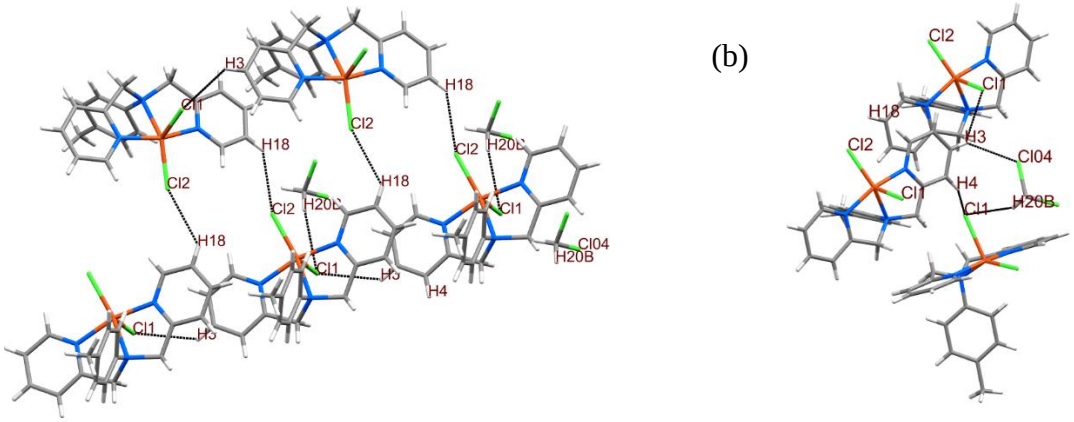

Fig. S15. (a) and (b) show the internuclear interactions present in the crystal structures of **1**.

(a) (b)

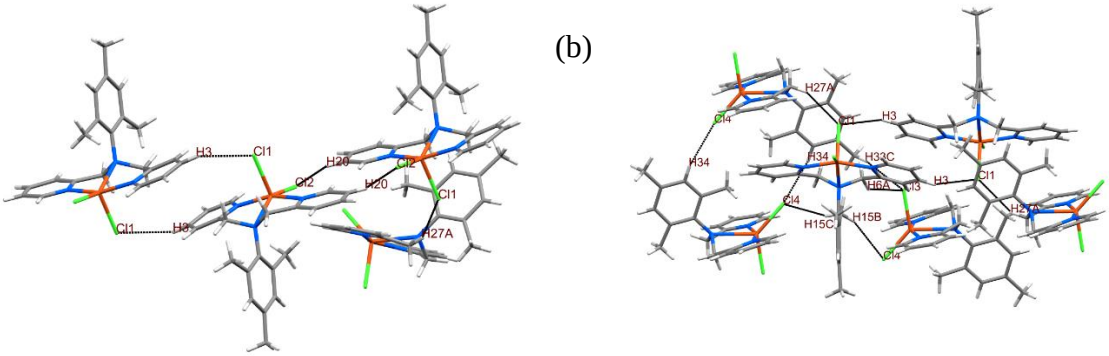

Fig. S16. Internuclear interactions present in the crystal structures of **2.**

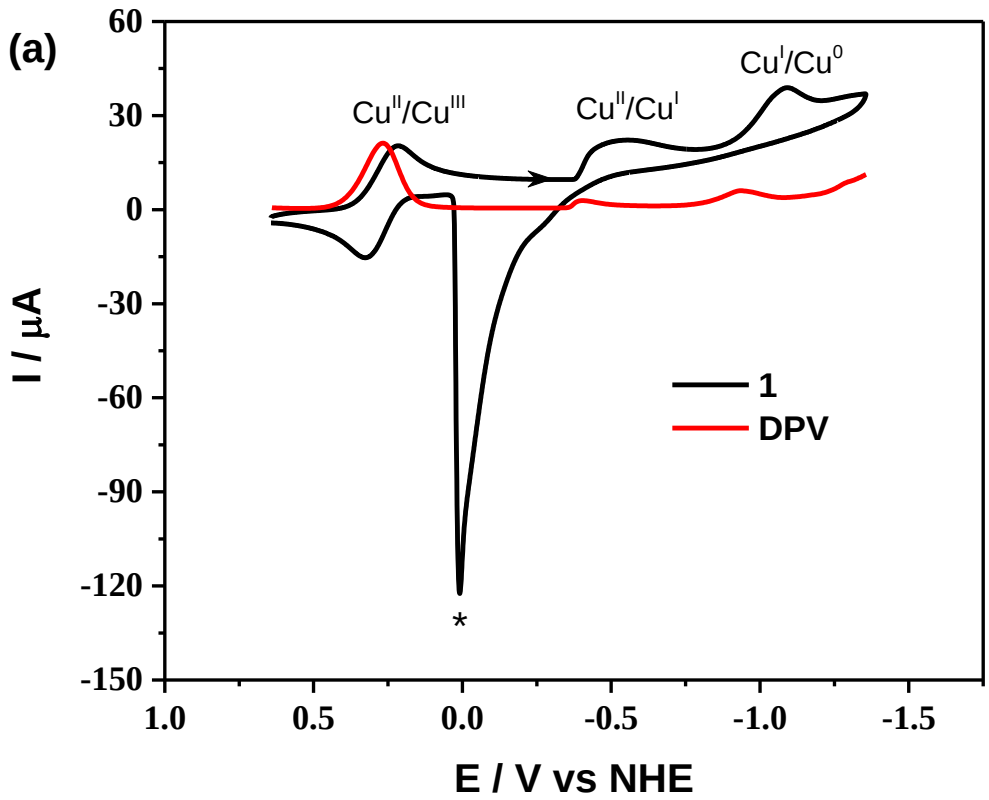

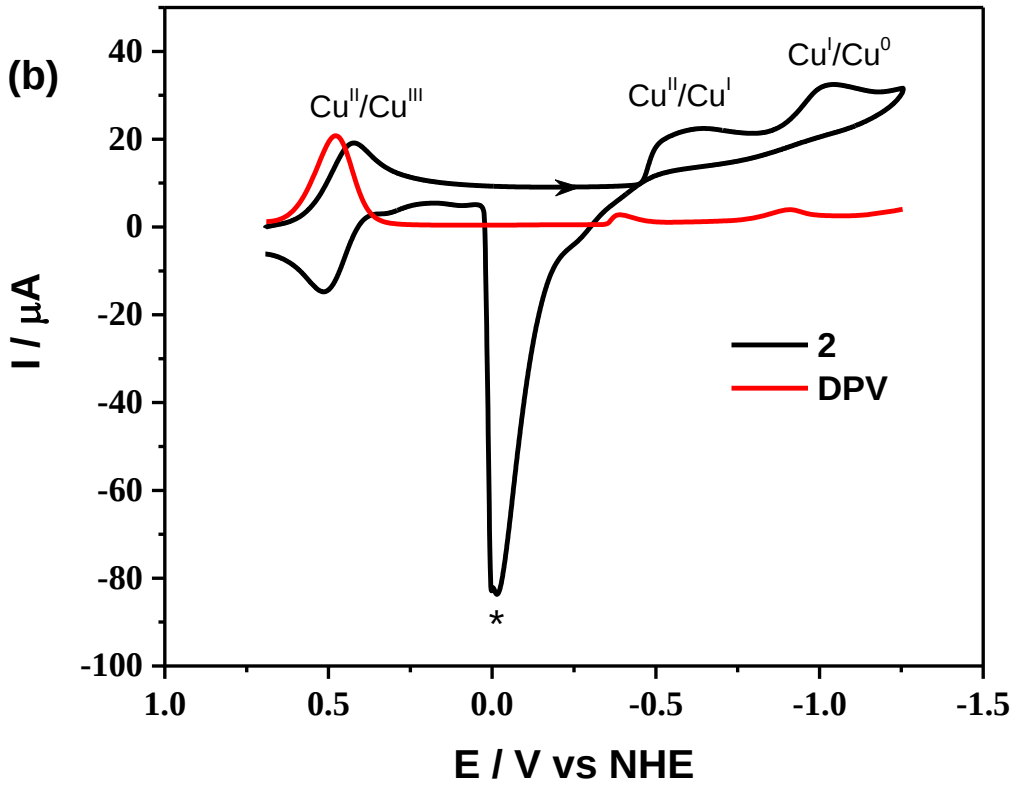

Fig. S17. CV and DPV of (a) **1** and (b) **2** in acetonitrile using 0.1 M TBAP as supporting electrolyte under argon atmosphere. The peak indicated by * is the deposited copper, for $Cu^0 \rightarrow Cu^I$ oxidation.

(a)

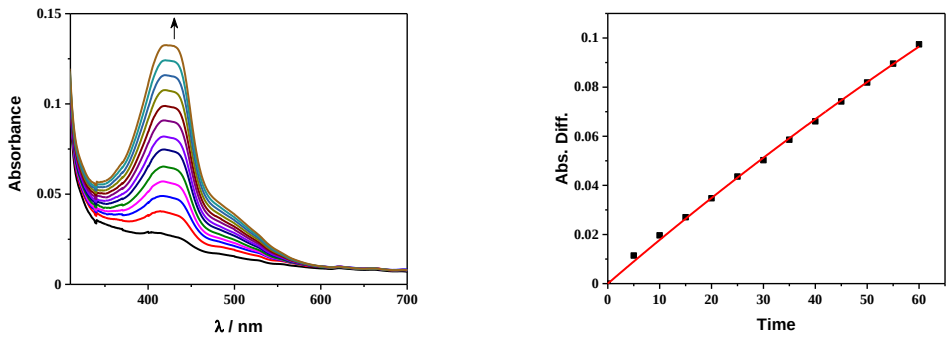

(b)

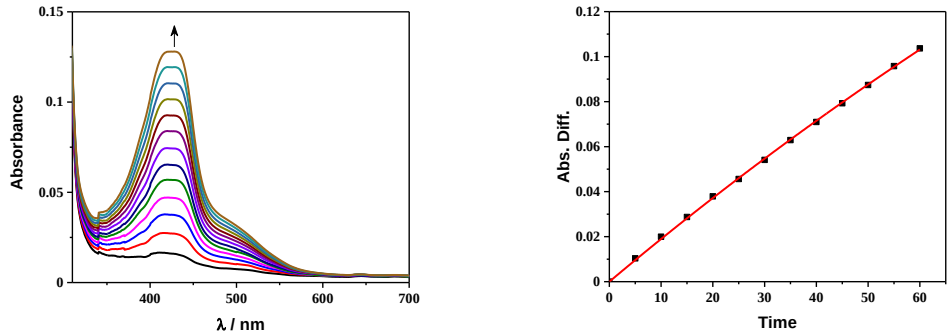

(c)

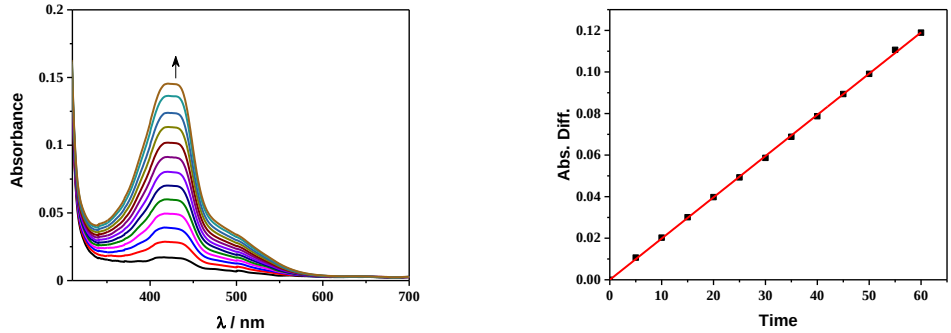

(d)

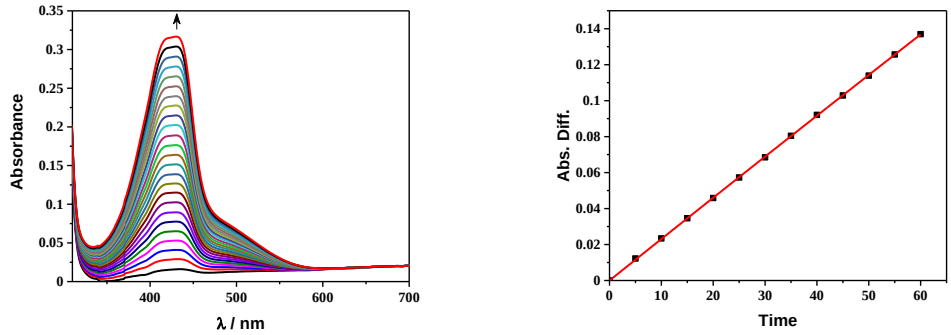

Fig. S18. Increase in phenoxazinone absorbance during the catalytic oxidation of (a) 0.25 × 10^{-2} M, (b) 0.50 × 10^{-2} M, (c) 0.75 × 10^{-2} M and (d) 1.00 × 10^{-2} M *o*-aminophenol with 1 × 10^{-4} M complex **1** at room temperature (25 °C) (left) and respective rate constant determination (right).

(a)

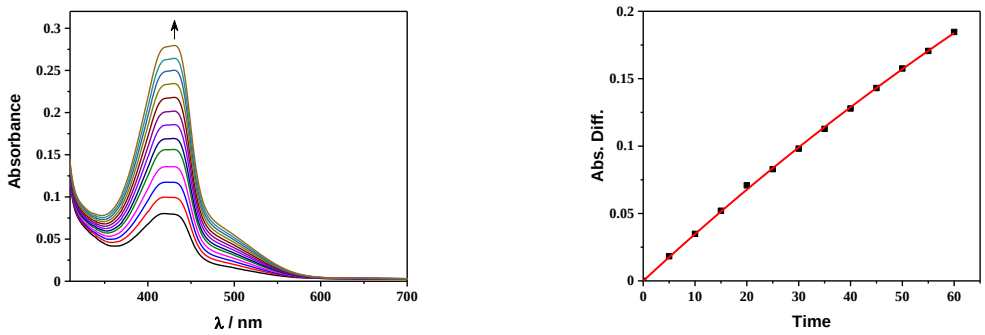

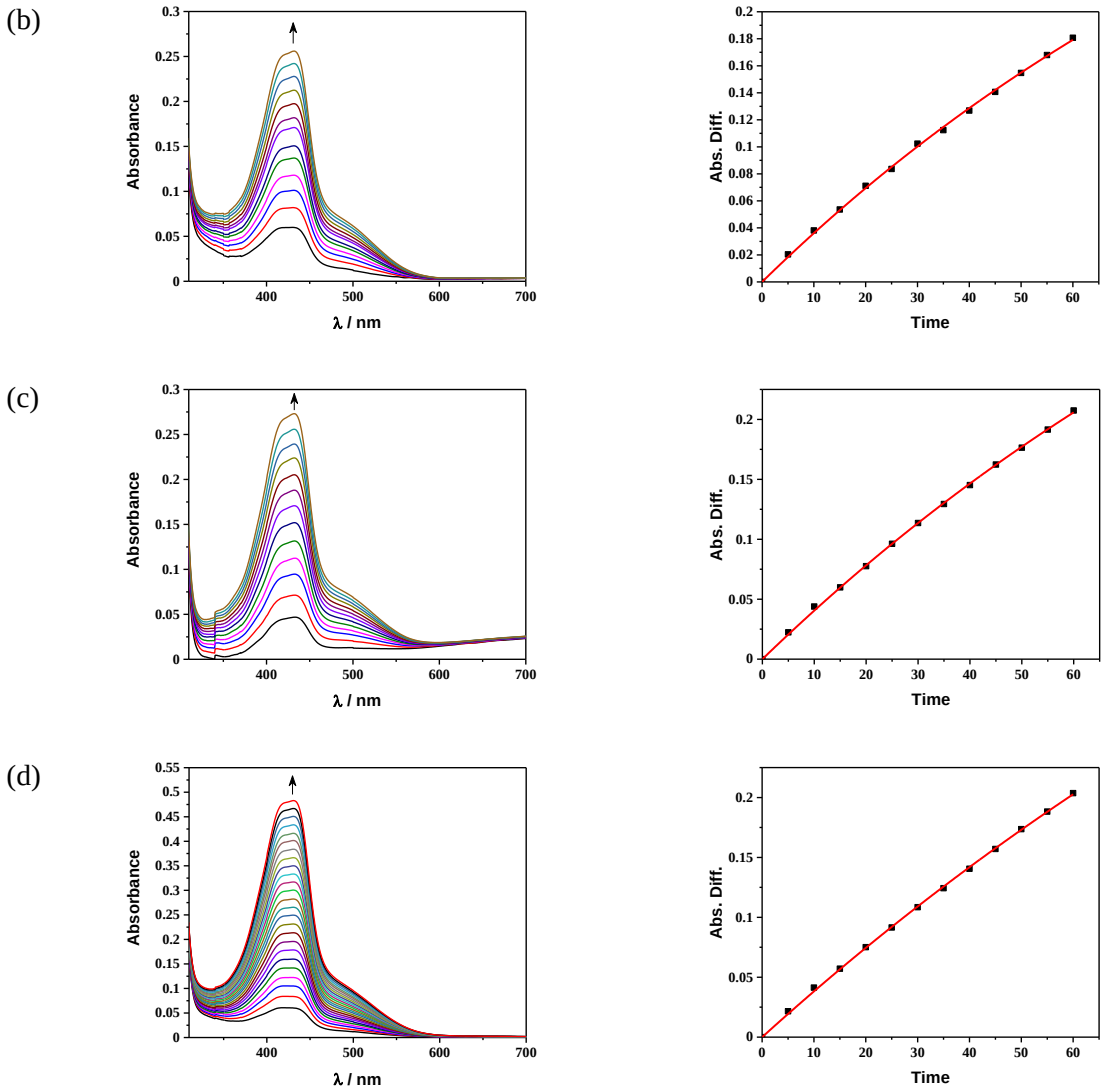

Fig. S19. Increase in phenoxazinone absorbance during the catalytic oxidation of (a) 0.25 × 10^{-2} M, (b) 0.50 × 10^{-2} M, (c) 0.75 × 10^{-2} M and (d) 1.00 × 10^{-2} M *o*-aminophenol with 1 × 10^{-4} M complex **2** at room temperature (25 °C) (left) and respective rate constant determination (right).

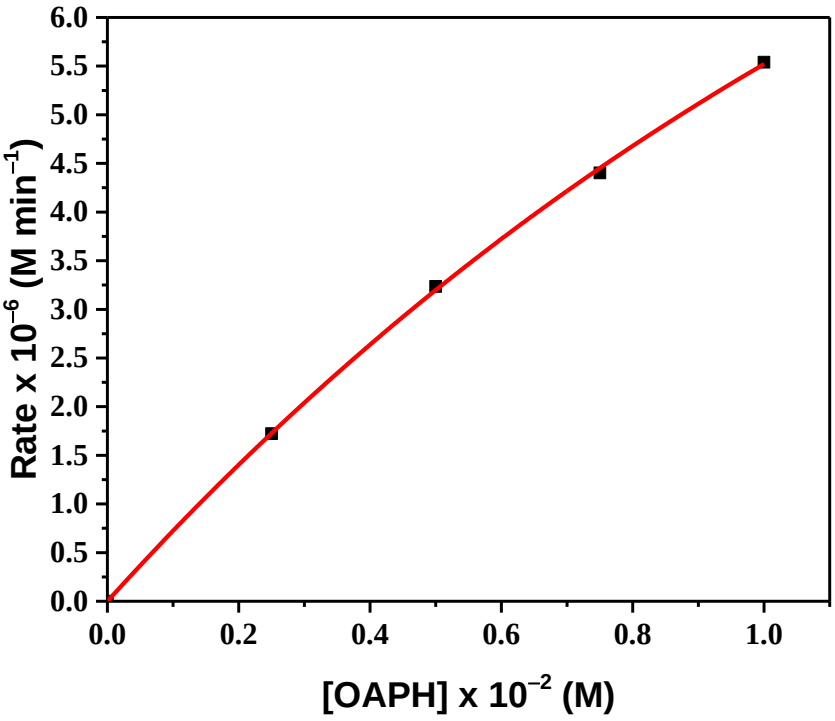

Fig. S20. Initial rate *versus* substrate concentration plot for the oxidation of *o*-aminophenol catalysed by **2** at room temperature (25 °C).

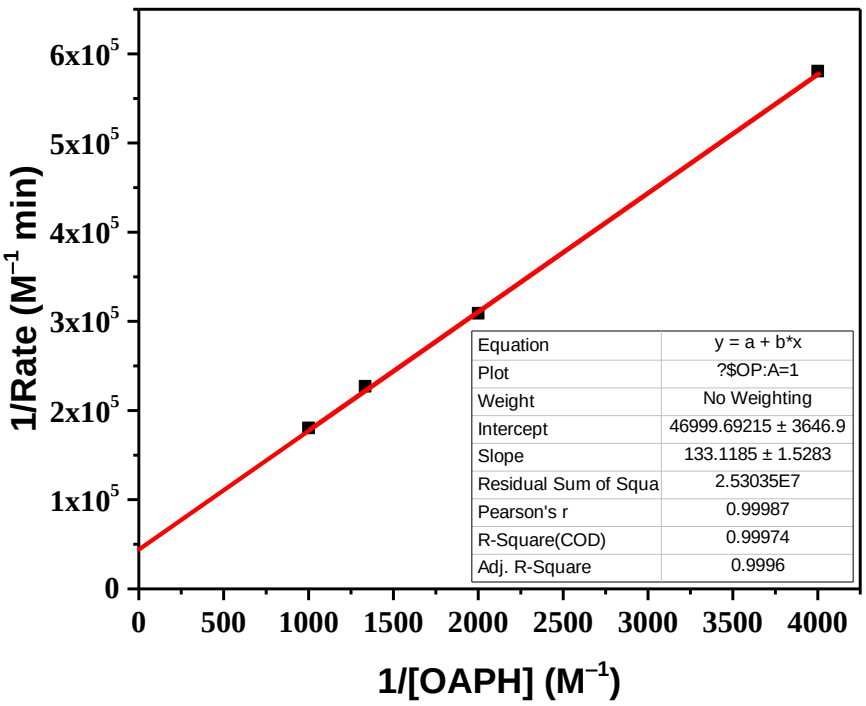

Fig. S21. Lineweaver-Burk plots for the oxidation of *o*-aminophenol catalysed by **2** at room temperature (25 °C).

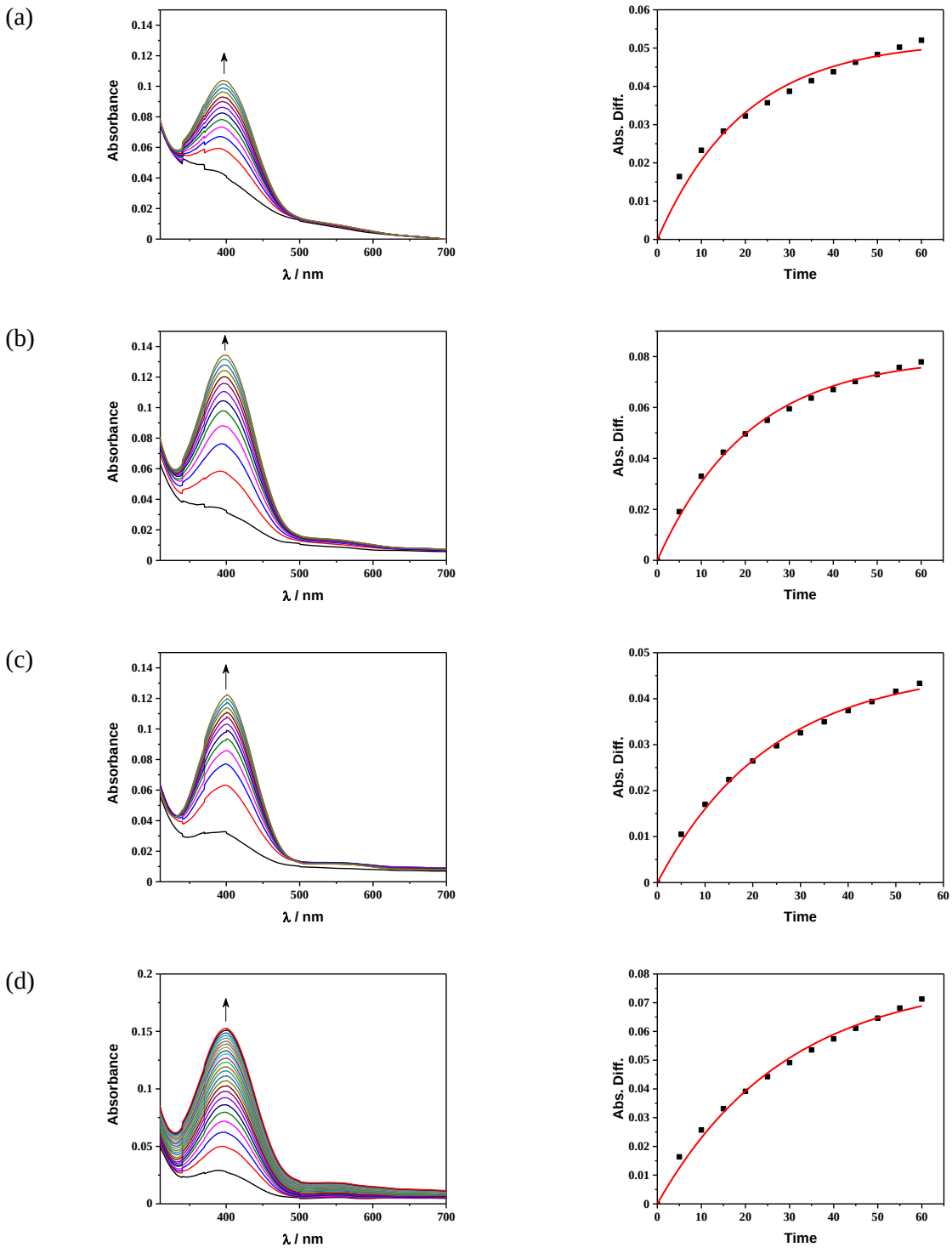

Fig. S22. Increase in quinone absorbance during the catalytic oxidation of (a) 0.25 × 10^{-3} M, (b) 0.50 × 10^{-3} M, (c) 0.75 × 10^{-3} M and (d) 1.00 × 10^{-3} M 3,5-DTBC with 1 × 10^{-5} M complex **1** at room temperature (25 °C) (left) and respective rate constant determination (right).

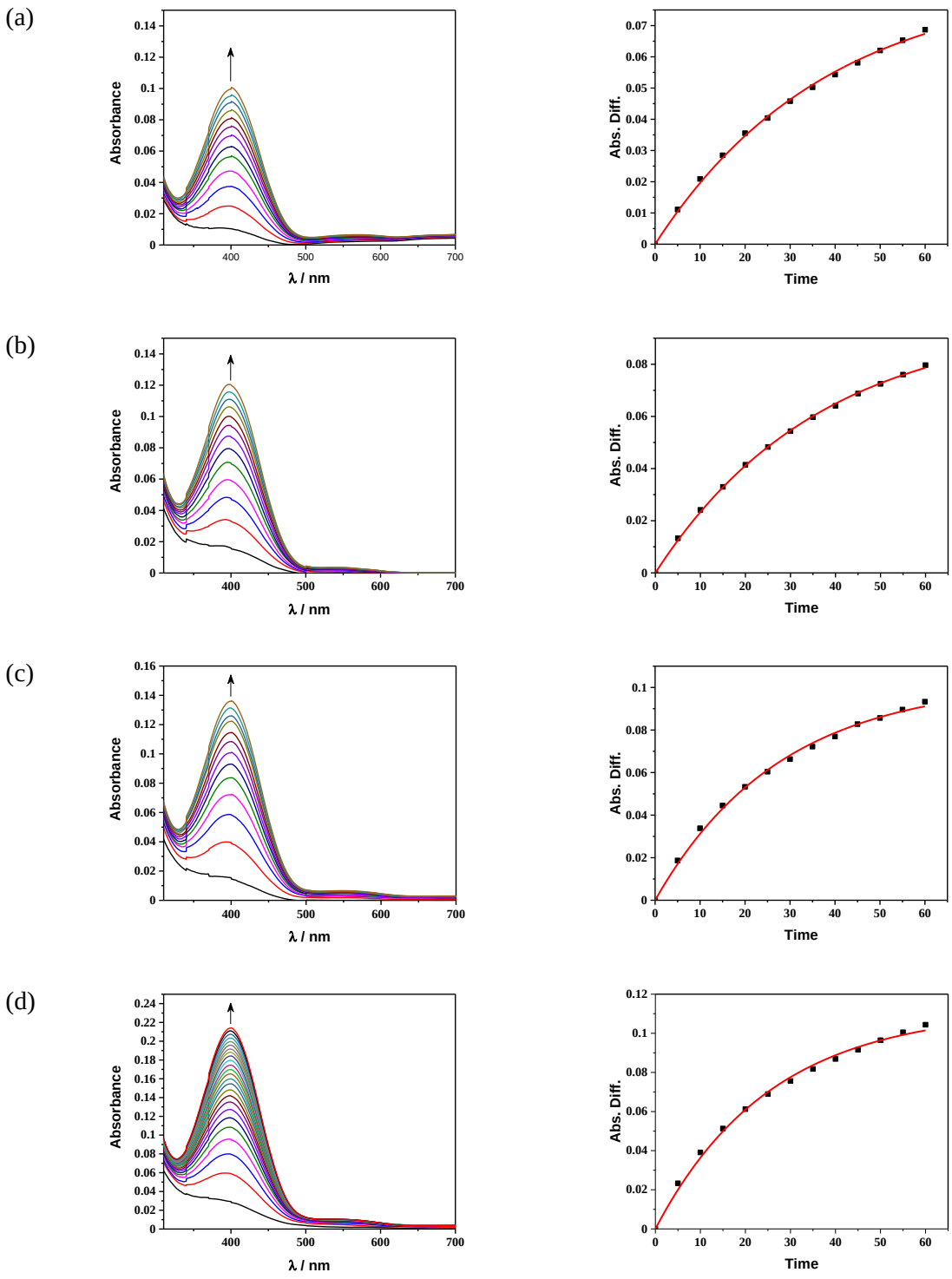

Fig. S23. Increase in quinone absorbance during the catalytic oxidation of (a) 0.25 × 10^{-3} M, (b) 0.50 × 10^{-3} M, (c) 0.75 × 10^{-3} M and (d) 1.00 × 10^{-3} M 3,5-DTBC with 1 × 10^{-5} M complex **2** at room temperature (25 °C) (left) and respective rate constant determination (right).

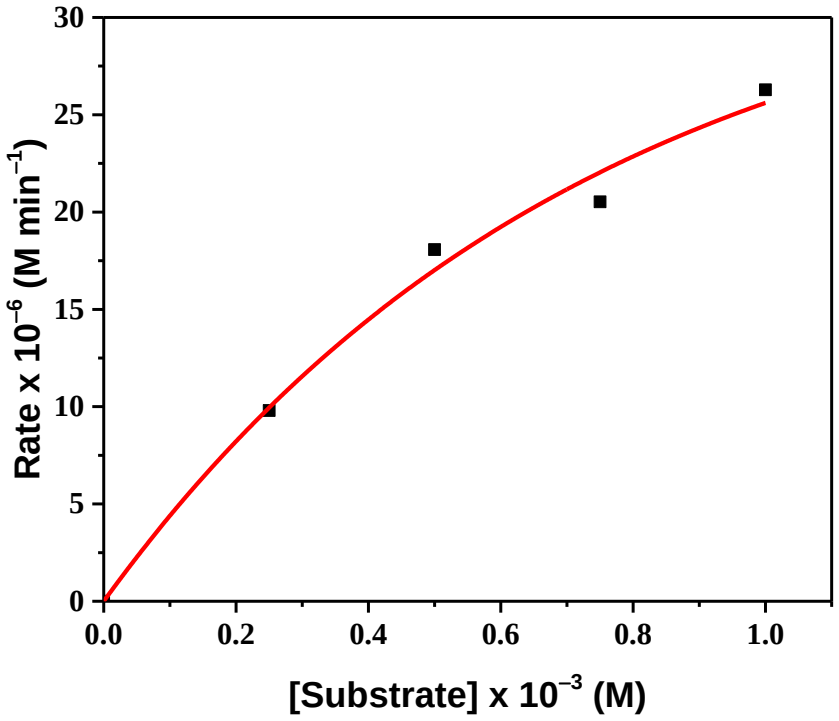

Fig. S24. Initial rate *versus* substrate concentration plot for the oxidation of 3,5-DTBC catalysed by **2** at room temperature (25 °C).

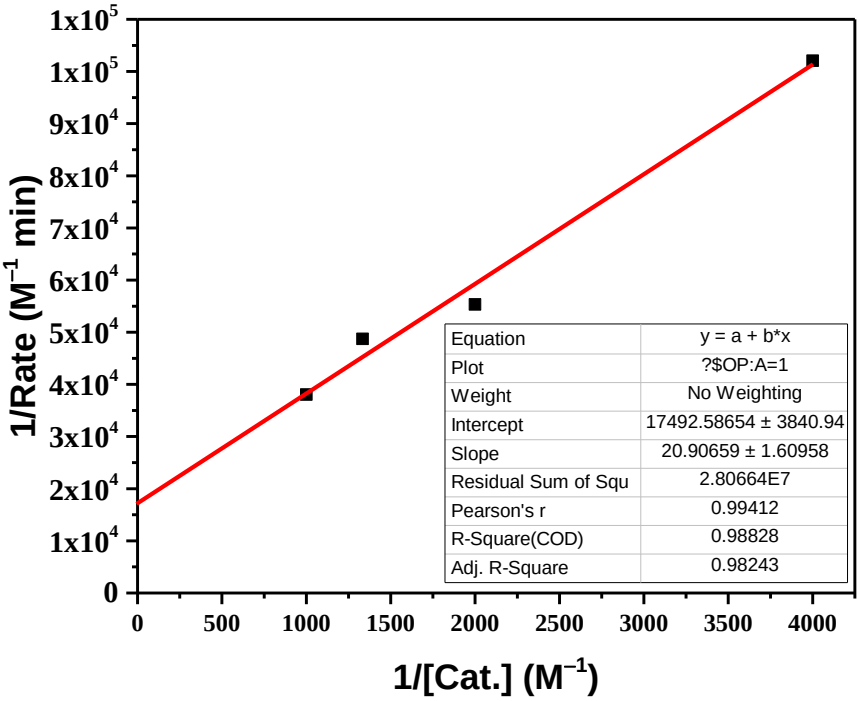

Fig. S25. Lineweaver-Burk plots for the oxidation of 3,5-DTBC catalysed by **2** at room temperature (25 °C).

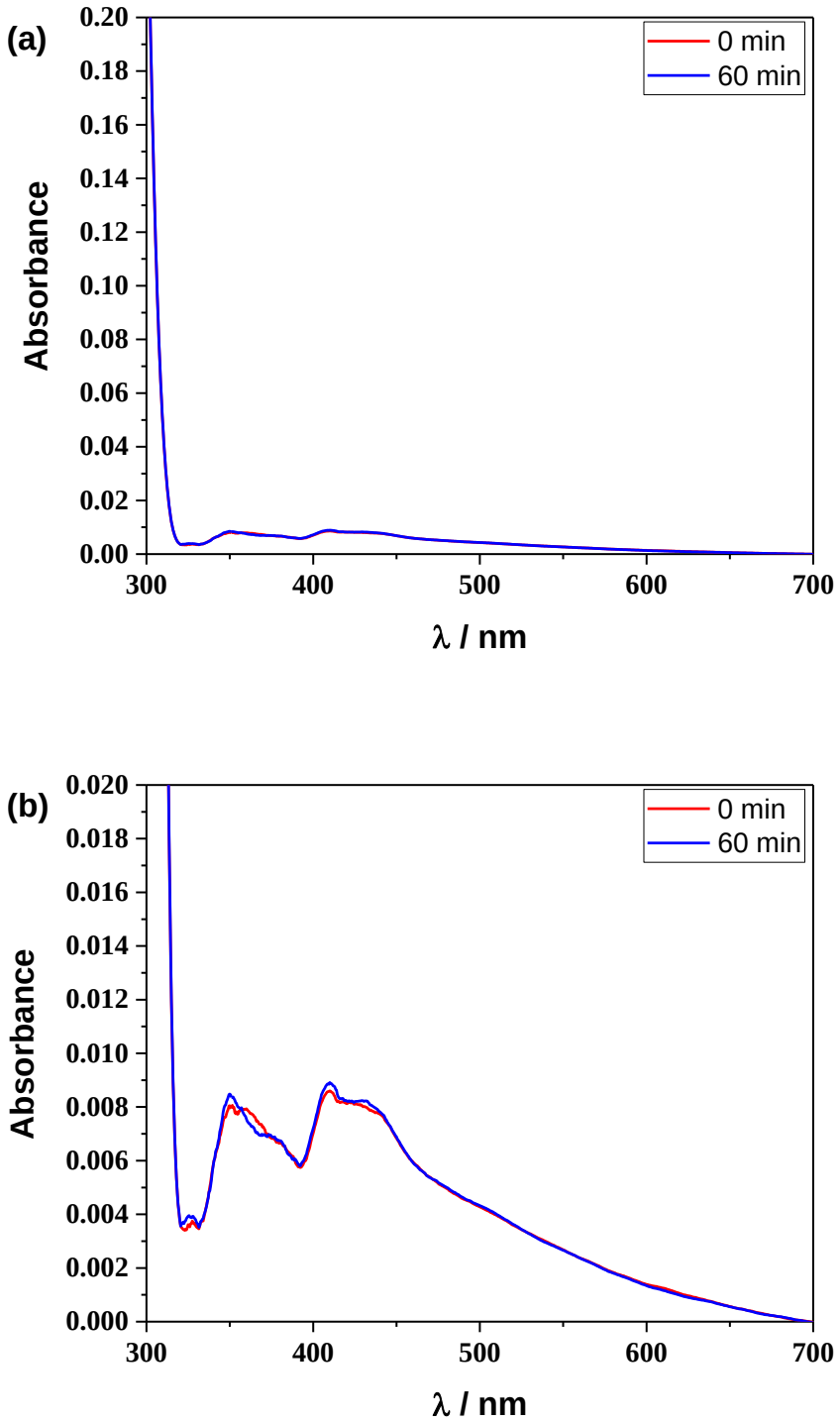

Fig. S26. *o*-aminophenol oxidation of 1×10^{-2} M substrate in methanol only (blank test) at room temperature (25 °C) (a) and zoomed version (b).

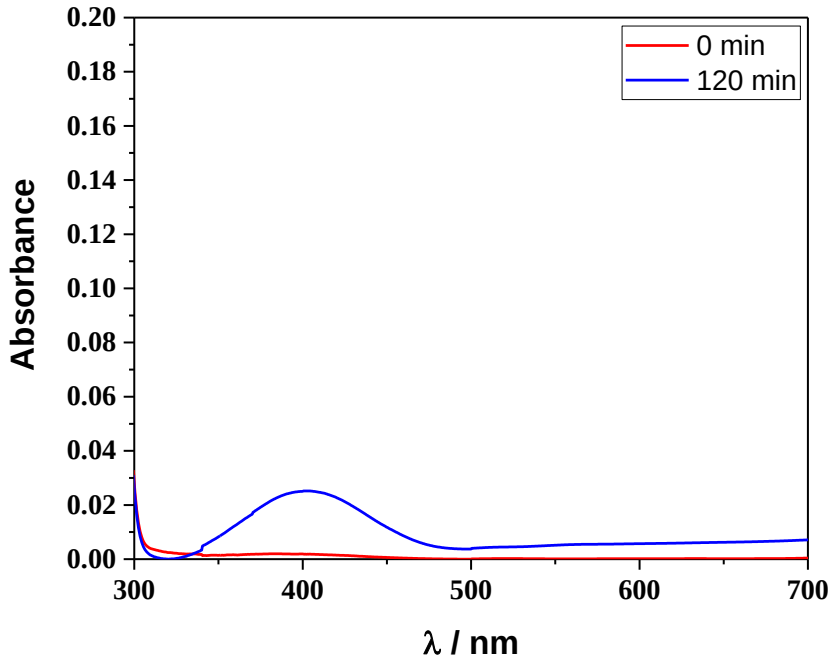

Fig. S27. 3,5-DTBC oxidation of 1×10^{-3} M substrate in methanol only (blank test) at room temperature (25 °C).

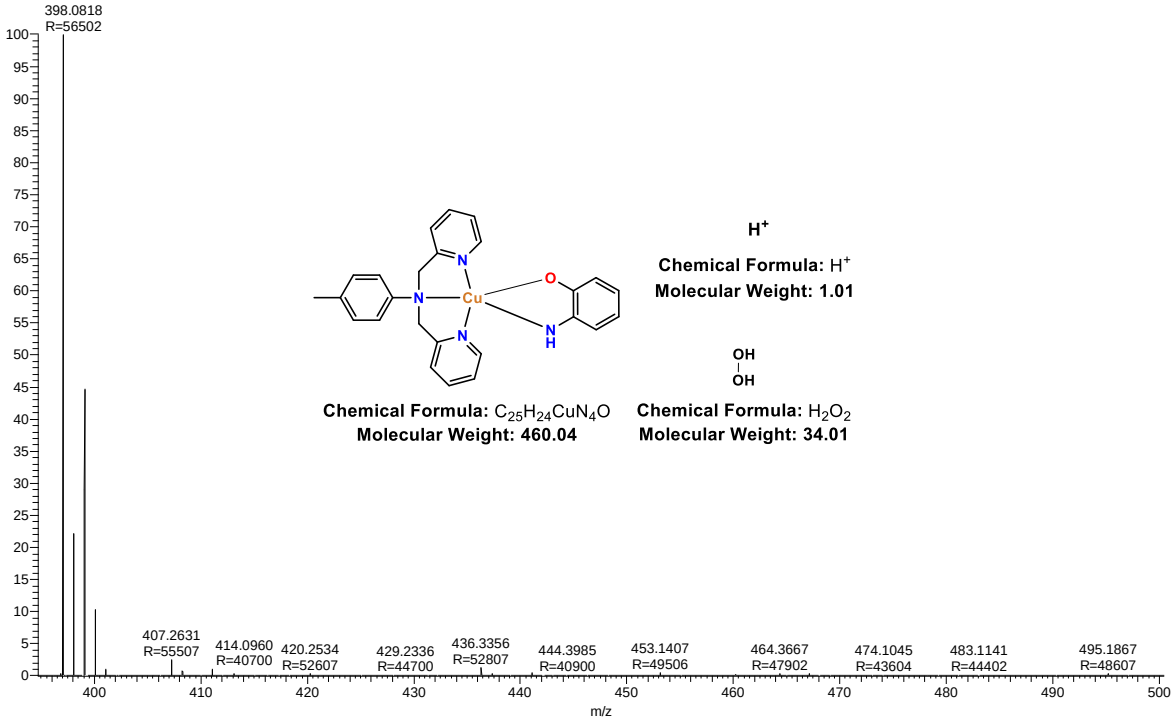

Fig. S28. Evidence of adduct formation along with peroxide in case of *o*-aminophenol oxidation catalysed by **1** found via mass spectrometry.

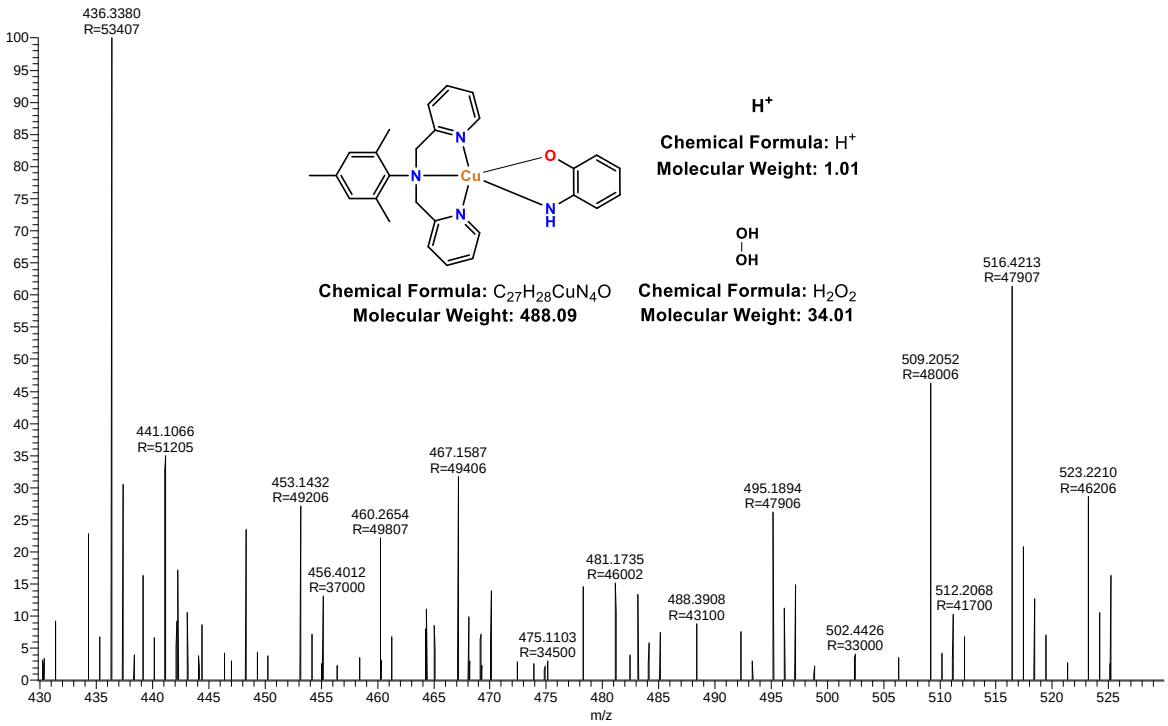

Fig. S29. Evidence of adduct formation along with peroxide in case of *o*-aminophenol oxidation catalysed by **2** found via mass spectrometry.

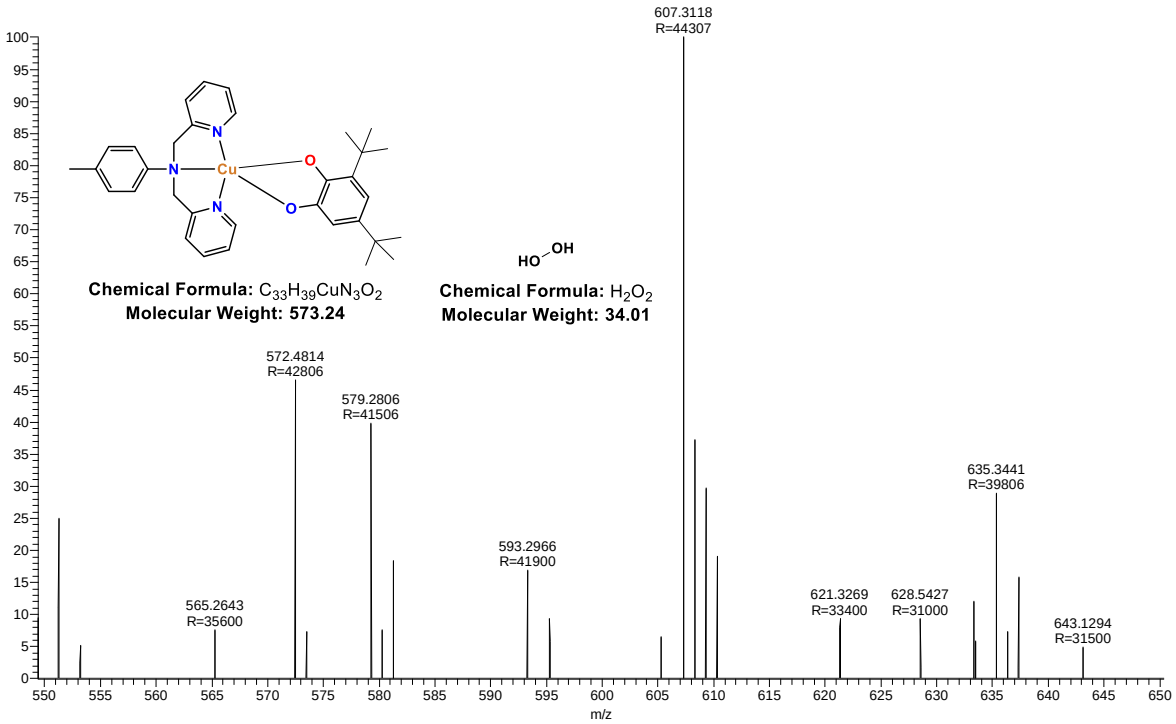

Fig. S30. Evidence of adduct formation along with peroxide in case of 3,5-DTBC oxidation catalysed by **1** found via mass spectrometry.

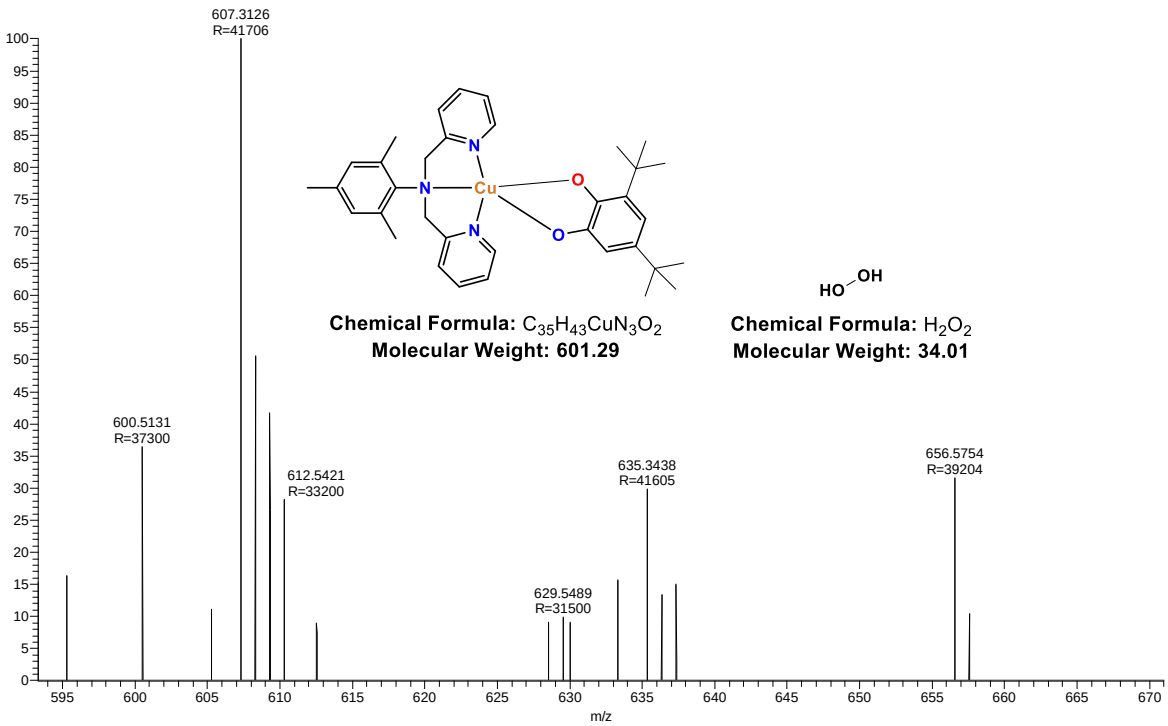

Fig. S31. Evidence of adduct formation along with peroxide in case of 3,5-DTBC oxidation catalysed by **2** found via mass spectrometry.

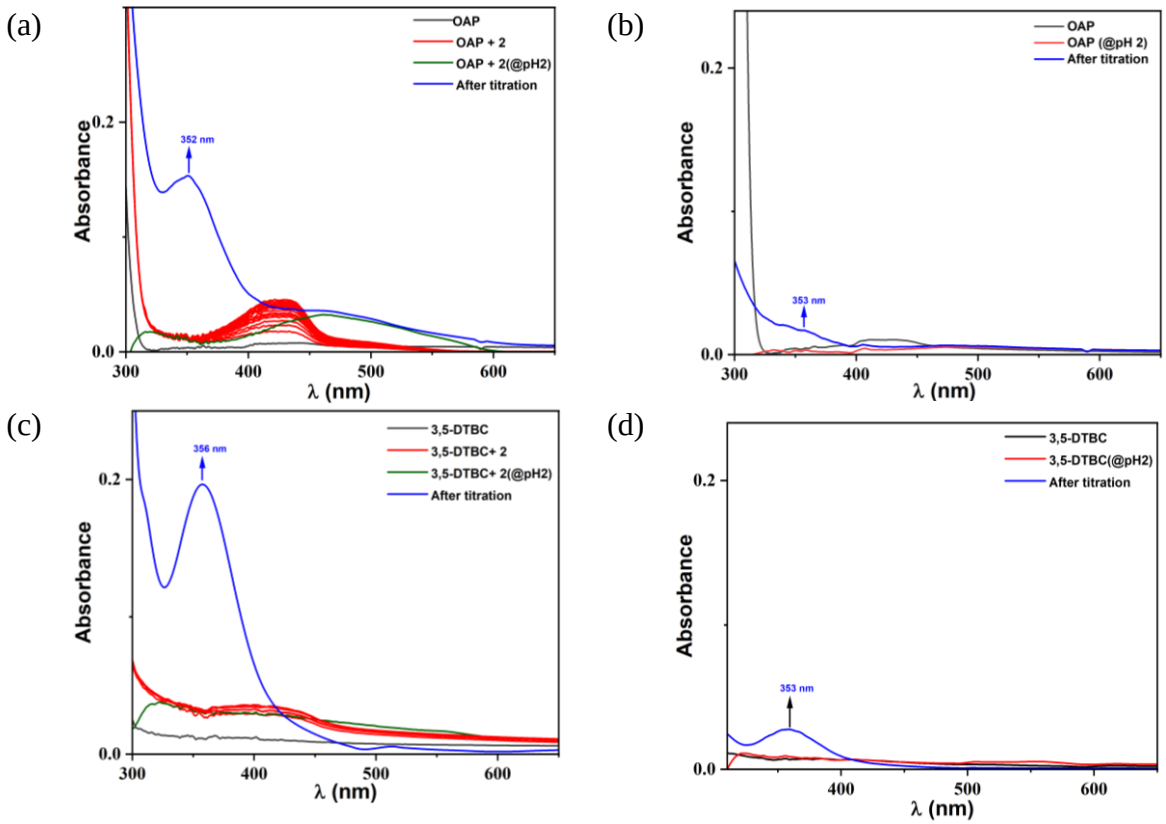

Fig. 32. Iodometric titration for the detection of H_2O_2 in case of (a) *o*-aminophenol and (c) 3,5-DTBC with **2** at 25 °C. (b) and (d) denotes the respective control experiments.

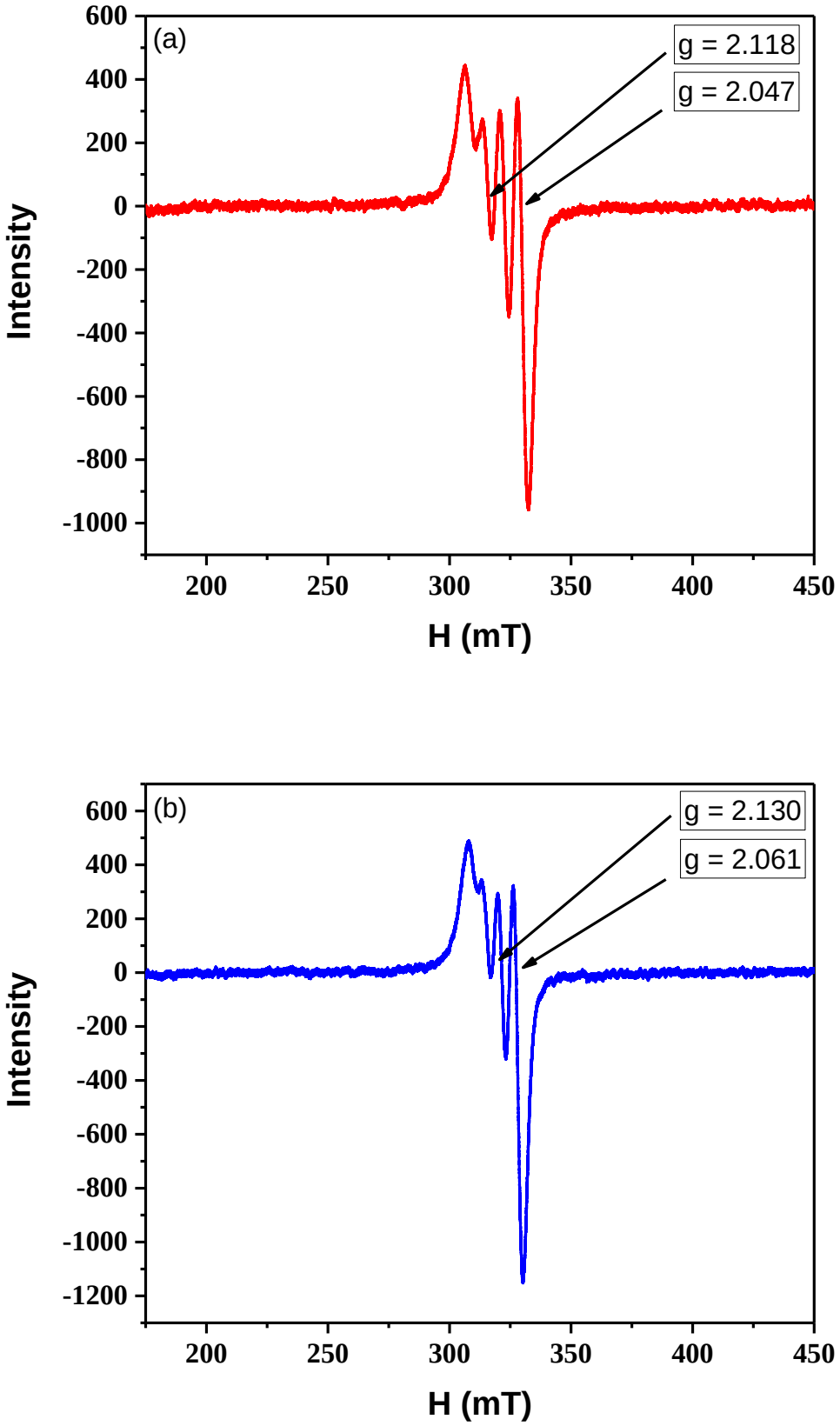

Fig. S33. EPR spectra of (a) 10:1 3,5-DTBC with **1** in methanol and (b) 10:1 3,5-DTBC with **2** in methanol at 298 K.